

Spatial, seasonal and solar cycle variations of the Martian total electron content (TEC): Is the TEC a good tracer for atmospheric cycles?

Beatriz Sánchez-Cano¹, Mark Lester¹, Olivier Witasse², Pierre-Louis Blelly³, Mikel Indurain³, Marco Cartacci⁴, Francisco González-Galindo⁵, Álvaro Vicente-Retortillo⁶, Andrea Cicchetti⁴, Raffaella Noschese⁴

¹ Radio and Space Plasma Physics Group, Department of Physics and Astronomy, University of Leicester, University Road, Leicester, LE1 7RH, UK.

² European Space Agency, ESTEC – Scientific Support Office, Keplerlaan 1, Noordwijk 2200 AG, The Netherlands.

³ Institut de Recherche en Astrophysique et Planétologie (IRAP), Toulouse, France.

⁴ Istituto Nazionale di Astrofisica (INAF), Istituto di Astrofisica e Planetologia Spaziali (IAPS), Rome, Italy.

⁵ Instituto de Astrofísica de Andalucía, CSIC, Granada, Spain

⁶ Department of Climate and Space Sciences and Engineering, University of Michigan, Ann Arbor, Michigan, USA

Corresponding author: Beatriz Sánchez-Cano (bscmdr1@leicester.ac.uk)

Key Points:

- The spatial, seasonal, and solar cycle variation of 10 years of Mars' TEC is assessed
- Mars Express routinely measures the dynamic of the thermosphere-ionosphere coupling
- The TEC can be used as a tracer for atmospheric cycles on the upper atmosphere

Key Words:

Atmospheric coupling, Mars ionosphere, Mars thermosphere, ionosphere modelling, Mars Express

This is the author manuscript accepted for publication and has undergone full peer review but has not been through the copyediting, typesetting, pagination and proofreading process, which may lead to differences between this version and the [Version of Record](#). Please cite this article as doi: [10.1029/2018JE005626](https://doi.org/10.1029/2018JE005626)

1 **Abstract**

2 We analyze 10 years of Mars Express total electron content (TEC) data from the Mars Advanced
3 Radar for Subsurface and Ionospheric Sounding (MARSIS) instrument. We describe the spatial,
4 seasonal, and solar cycle behavior of the Martian TEC. Due to orbit evolution, data come mainly
5 from the evening, dusk terminator and post-dusk nightside. The annual TEC profile shows a
6 peak at $L_s=25^\circ-75^\circ$ which is not related to the solar irradiance variation, but instead coincides
7 with an increase in the thermospheric density, possibly linked with variations in the surface
8 pressure produced by atmospheric cycles such as the CO_2 or water cycles. With the help of
9 numerical modelling, we explore the contribution of the ion species to the TEC and the coupling
10 between the thermosphere and ionosphere. These are the first observations which show that
11 the TEC is a useful parameter, routinely measured by Mars Express, of the dynamics of the
12 lower-upper atmospheric coupling, and can be used as tracer for the behavior of the
13 thermosphere.

14 **Plain Language Summary**

15 Ten years of Mars Express total electron content (TEC) data from the Mars Advanced Radar for
16 Subsurface and Ionospheric Sounding (MARSIS) instrument are analyzed. The TEC is a
17 parameter that gives information of the amount of free electrons within the ionosphere (ionized
18 layer at $\sim 100-200$ km). In this study, we describe how the TEC varies along the seasons, planet
19 coverage and also, with the solar activity. We have found that variations in the thermosphere
20 (neutral atmospheric layer between 100 and 200 km) have an effect on the ionosphere,
21 especially notable during spring of the northern hemisphere. With the help of a numerical
22 simulation of the ionosphere-thermosphere over a Martian year, we have found that Mars'
23 atmospheric cycles can have an effect on the upper atmosphere.

24 1. Overview

25 The Martian total electron content (TEC) has been the topic of several studies in recent times
26 because of its potential to monitor the Martian ionospheric behavior [e.g. Morel et al., 2004;
27 Safaeinili et al. 2007; Lillis et al., 2010; Cartacci et al., 2013; 2018; Mendillo et al., 2013; 2015;
28 2017a, 2017b; Sánchez-Cano et al., 2015a; 2016]. The TEC represents the number of free
29 electrons that are contained along the path between a radio transmitter and receiver. TEC at
30 Mars is typically retrieved as a by-product of the analysis of the signal distortion caused by the
31 dispersion that the ionosphere produces [e.g. Safaeinili et al. 2007; Mouginot et al., 2008;
32 Cartacci et al., 2013]. The above studies outlined the ionospheric variability, and also
33 highlighted the difficulty of relying on a very precise absolute number for the TEC at low solar
34 zenith angles (SZA) on the pure dayside due to its dense ionosphere using the current radars at
35 Mars, which have operating frequencies close to the peak plasma frequency.

36 Despite the progress made in the last decade, we still do not fully understand the long-term
37 evolution of the ionospheric behavior in relation to the thermospheric variability. The
38 ionosphere and thermosphere are obviously coupled because the ionosphere is formed by solar
39 photo-ionization of the upper atmospheric neutral layer, and governed by a variety of complex
40 non-linear chemical, dynamical, electrodynamical, and radiative processes [Yigit et al., 2016].
41 The structure of the atmosphere-ionosphere system is influenced by several external and
42 internal forcing processes, e.g., space weather, crustal magnetic fields, or gravity waves among
43 many others. New evidence demonstrates that different regions of the Martian atmosphere are
44 fundamentally interconnected, and behave as a unique coherent system [e.g. Jakosky, 2015;
45 Bougher et al., 2015; 2017; Montmessin et al., 2017]. This means that the whole atmospheric
46 structure reacts together to external and internal sources of variability on different time and
47 space scales. This is a growing topic largely unexplored so far.

48 In this study, we go one step further in order to assess whether the TEC is a useful tracer for the
49 Martian thermosphere, and eventually, whether TEC can be used as a diagnostic parameter of
50 the coupling between the lower and upper atmosphere. Specifically, we look into spatial,
51 seasonal and solar cycle effects of ~6 Martian years (~10 Earth years) of TEC observations from
52 the Mars Advanced Radar for Subsurface and Ionospheric Sounding (MARSIS) instrument
53 [Picardi et al., 2004; Orosei et al., 2015] on board the Mars Express (MEX) mission, which has
54 been in orbit about Mars since December 2003 [Chicarro et al., 2004].

55 This paper is divided as follows. In Section 2, the general seasonal behavior of several relevant
56 datasets for this study is described. In Sections 3 and 4, the seasonal ionosphere-thermosphere
57 coupling after considering the effect of the solar cycle is assessed for mid and polar latitudes,
58 respectively. In Section 5, a numerical simulation of the ionosphere is performed in order to
59 help with the data interpretation. The simulation outlines the coupling between the ionosphere
60 and the thermosphere as seen by the TEC observations. Finally, in Section 6, the effect of the
61 long-term coupling between the lower and upper atmospheres on the TEC is investigated, as
62 this connection is much stronger than on Earth because Mars does not have a permanent
63 stratosphere [e.g. González-Galindo et al. 2008].

64 2. General Observations

65 The ionosphere is characterized by a dynamic balance in which the net density of free electrons
66 is described by the continuity equation, which depends on the relative speed of ion production
67 and loss processes, and plasma transport [Chapman and Bartels, 1940]. In addition, the ion
68 production and ion losses depend on the intensity of the incoming solar radiation and on the
69 density and chemistry of the neutral atmosphere [e.g. Witasse et al., 2008]. At Earth, the solar
70 flux is considered the dominant factor of ionization since the mass of the neutral atmosphere
71 column, on average, does not vary significantly over a year for a given location. At Mars, beyond
72 the irradiance flux, the thermosphere has a particular semiannual variation which may also
73 have an influence on the ionospheric behavior with seasons, as we show in this section.

74 Figure 1 shows different ionospheric-atmospheric observations from several Martian years
75 (MY) that have been averaged together and plotted with respect to the solar longitude (Ls),
76 which can be used as a proxy for the Martian year. Each parameter in Figure 1 has been
77 averaged within Ls bins of 10° . We note that results shown in this figure are not an artifact of
78 the Ls binning process, because after using different sizes of Ls binning, similar results were
79 obtained.

80 Figure 1a shows the averaged MARSIS TEC observations from ~ 6 MY (MY mid 27-32, mid-2005
81 to mid-2015) for a SZA of $85^\circ (\pm 0.5^\circ)$. MARSIS TEC data come from its subsurface operational
82 mode [Safaeinili et al., 2007]. In this mode, the TEC is routinely estimated from the frequency
83 phase shift caused by the ionosphere to the radar signals traveling from the spacecraft to the
84 ground and vice versa [e.g. Sánchez-Cano et al., 2015a]. TEC was obtained through the Cartacci
85 et al. [2013] algorithm, after only considering data with a Signal-to-Noise Ratio (SNR) larger
86 than 20 dB, and only considering data from the two larger MARSIS frequencies, i.e., 4 and 5
87 MHz. This conservative approach guarantees good quality data. We note that the SZA chosen in
88 Figure 1a corresponds to a region near the terminator of the day. This is because the MARSIS

89 radar in the subsurface mode is usually not operated on the full dayside due to low radar
90 performance [Sánchez-Cano et al., 2015a], and, therefore, accurate TEC observations in the
91 dayside are limited to high SZA. Moreover, the majority of the MARSIS data from $SZA=85^\circ$
92 comes from the dusk sector, local time (LT) ~ 18 h, due to the MEX orbit evolution and
93 observation planning priorities. In an early MARSIS work with TEC data from 2005-2006,
94 Safaeinili et al. [2007] showed that the ionosphere of Mars has a significant local time
95 asymmetry. Unfortunately due to the Mars Express orbit trajectory and science operation
96 planning constrains and priorities over the subsequent years, it is not possible to do a similar
97 analysis because the MARSIS dusk coverage is $\sim 88\%$ of the full dataset, while the dawn
98 coverage is only $\sim 12\%$. Therefore, we consider that our results are not affected by the local
99 time asymmetry, even if such asymmetry does exist [Safaeinili et al., 2007]. Moreover, it is well-
100 known that the terminators are regions of localized high thermospheric variability [Zurek et al.,
101 2017], the local time asymmetry is masked in this study as we statistically analyze 6 MY of TEC
102 data together to assess the long-term evolution of the total ion and electron columns. Figure 1b
103 shows the averaged atmospheric density at 140 km above the planet's surface (the
104 approximate altitude of the maximum ionization region of the ionosphere) obtained from the
105 Mars Climate Database (MCD). The MCD (version 5.3) is a meteorological database built from a
106 Global Circulation Model (GCM) of the Martian atmosphere, called Laboratoire de Meteorologie
107 Dynamique (LMD) model, and widely validated with observational data [e.g. Forget et al., 1999;
108 Millour et al., 2015]. The MCD considers the CO_2 , water and dust cycles [Forget et al., 1998;
109 Madeleine et al., 2012; Navarro et al., 2014] along with other meteorological conditions of each
110 Martian year. In our case, Figure 1b shows the averaged results obtained from the MCD for the
111 same period of the MARSIS TEC data (MY27-MY32), and after averaging the results from six
112 equispaced different latitudes that cover the full planet. These data were obtained only at
113 $LT=18$ h, which corresponds to $\sim SZA=85^\circ$, i.e. the same condition as for the MARSIS TEC
114 observations (Figure 1a), and with the actual solar flux conditions of those years. Figure 1c
115 shows the global averaged thermospheric column density profile between 100 and 200 km
116 altitude (i.e. the thermosphere) for each of the major species: hydrogen (H), atomic oxygen (O),
117 molecular nitrogen (N_2), molecular oxygen (O_2) and carbon dioxide (CO_2). This figure does not
118 show the relative abundances of the neutral species, but instead, it shows the temporal
119 variability of each species, which has been normalized to its value at $Ls=355^\circ$ in order to
120 visualize all species on the same scale. Since the solar flux effect on the thermosphere can mask
121 the annual variation of the neutral species, these profiles were obtained from the MCD after
122 assuming a constant solar flux, as will be described in detail in the Section 5. Figure 1d shows
123 the daily averaged surface pressure measured by the Rover Environmental Monitoring Station
124 (REMS) instrument [Gómez-Elvira et al. 2012] onboard the Mars Science Laboratory (MSL)

125 mission [Grotzinger et al. 2012]. The time span of this panel covers the ~3 Martian years that
126 MSL has been working at the surface of Mars (MY mid 31-33, mid-2012 to beginning 2017).
127 MSL is located almost near the Martian equator, and therefore Figure 1d shows the averaged
128 variation of the surface pressure (as a proxy for the atmospheric mass column variation) at
129 almost equal distance from both poles. Figure 1e shows the solar irradiance measured by the
130 Thermosphere, Ionosphere, Mesosphere Energetics and Dynamics (TIMED)-Solar EUV
131 Experiment (SEE) satellite [Woods and Eparvier, 2006] at a wavelength of 30.5nm, which is the
132 closest one measured by TIMED to the Helium 30.4nm intense line of the spectrum that causes
133 the major CO₂ ionization (main atmospheric component at Mars). The irradiance was measured
134 at 1 AU for the same MARSIS TEC period (MY27-MY32), and subsequently extrapolated to Mars
135 assuming that the irradiance was not significantly different in solar longitude when Earth and
136 Mars were in superior solar conjunction. Finally, Figure 1f shows the Mars' heliocentric
137 distance, illustrating aphelion at Ls=71° and perihelion at Ls=251°.

138 As expected, the TEC (Figure 1a) follows the irradiance profile well (Figure 1e) because the
139 solar flux is the dominant agent of ionization. The sinusoidal shape of both the irradiance and
140 the TEC is due to Mars' heliocentric distance (Figure 1f), as the solar flux diminishes with the
141 square of the heliocentric distance. Therefore, both the TEC and the irradiance maxima are
142 near Mars' perihelion and their minima near aphelion. However, the TEC profile shows a
143 secondary maximum between Ls=25° and 75° (Figure 1a), which is not related to the annual
144 irradiance variation (Figure 1e). This feature was previously visible in Figure 3 of Hall et al.
145 [2016], although its origin was not interpreted. This secondary peak occurs near the lowest
146 solar irradiance level at Mars (Figure 1e), during the northern spring season and before
147 aphelion, and nearly coincides with an increasing trend in both the thermospheric density
148 (Figures 1b and 1c) and the surface pressure (atmospheric mass, Figure 1d). As seen in Figure
149 1c, when the solar flux is fixed as a constant, O, O₂ and N₂ have their largest abundances in the
150 annual profile at this time of the year, indicating that these three components may have a more
151 prominent role during this period, as we later analyze in more detail. Therefore, it seems that
152 the thermosphere variability may play a role in the formation of this secondary TEC peak.

153 The main TEC peak (Ls=220°-290°) is also formed while there is an increase in the
154 thermospheric density and surface pressure (during spring in the southern hemisphere), which
155 is related to a larger abundance of CO₂, H, O₂ and N₂ with respect to their annual trends (Figure
156 1c). In this case, however, the solar irradiance is a maximum for this period (Figure 1e) and, is
157 the key factor in the formation of this TEC peak. As seen in Figure 1a, the absolute maximum of
158 the Martian year occurs at Ls=220°-240°, a few Ls degrees before the irradiance maximum at
159 Ls=251°. Although not conclusive, this could also be a result of a neutral atmospheric effect, as

160 the thermospheric conditions are similar to those regarding the first TEC peak, i.e., spring in the
161 southern hemisphere, increasing thermospheric density, and increasing surface pressure,
162 although with a much larger magnitude of the thermospheric density (Figure 1b) due to the
163 expansion of the atmosphere produced by the proximity to the Sun (Figure 1f). However, it is
164 difficult to evaluate whether there is an effect of the neutral atmosphere because the irradiance
165 flux is clearly the dominant ionization factor and masks any other secondary ionospheric
166 variability sources.

167 This overview figure demonstrates in a simple way the coherent long-term behavior of the
168 thermosphere-ionosphere coupling, in which atmospheric changes may produce significant
169 effects in the ionosphere formation. In the following section, we assess the long-term behavior
170 of this coupling.

171 **3. Ionosphere-Thermosphere Coupling: Mid-Low Latitudes**

172 In order to assess the seasonal variability of the thermosphere-ionosphere coupling with
173 latitude, SZA and solar cycle, we have split the MARSIS dataset by these parameters.

174 This section focuses only on TEC data from latitudes between -70° and 70° . Since Mars does not
175 have a global intrinsic magnetic field such as Earth, there is no need to distinguish between low
176 and mid latitudes because the ionospheric physics for all these latitudes is the same and can be
177 analyzed together. We do not split the dataset into smaller latitude bands because of data
178 coverage constraints. Despite the long mission time of MEX, and hence the large amount of TEC
179 data which have been acquired, there is a reduced latitude coverage in relation to the SZA
180 coverage in a Martian year. This is a direct consequence of the MEX orbit evolution.
181 Additionally, the MARSIS radar in subsurface mode only works during the ~ 30 min of the orbit's
182 periapsis, and when the SZA is high enough to avoid any radar signal losses due to a strong
183 dayside ionosphere [Cartacci et al., 2018]. Moreover, MARSIS switches between two operational
184 modes and so, it does not work in subsurface mode on all the orbits. For the same coverage
185 reason, we show every single TEC observation as a dot in Figure 2 and not binned as in the
186 previous figure.

187 In Figure 2, we present the TEC behavior of the Martian ionosphere in a year. The TEC data set
188 has been split into intervals of 5° of SZA (rows), starting from SZA= $[75^\circ, 80^\circ]$ and ending with
189 SZA= $[110^\circ, 115^\circ]$. In addition, the TEC dataset has been split into two different levels of solar
190 activity based on the solar cycle classification made by Sánchez-Cano et al. [2015b; 2016]. The
191 left column contains data from the low and medium solar activity phases of the solar cycle (MY
192 mid-27 to mid-30, mid-2005 to early 2011), and the right column contains data from the high

193 solar activity phase (MY mid-30 to 32, beginning-2011 to mid-2015). In order to achieve the
194 best data coverage in each panel, the low and mid solar cycle phases in Sánchez-Cano et al.
195 [2015b; 2016] are considered as “low” in this work. This approximation is realistic as the solar
196 irradiance levels were close enough during these three periods and remarkably different from
197 the high solar activity phase (see Sánchez-Cano et al. [2016], Figure 1).

198 Data in each panel of Figure 2 have been fitted with a 5th-degree polynomial curve (black dashed
199 line) to visualize their averaged annual trend. The 5th order polynomial has been chosen
200 because it is the one that best reproduces the double TEC asymmetric peak shape, but its
201 purpose is merely visual. Due to several data gaps between Ls 0° and 40°, the peak before
202 aphelion (Ls~71°) is not visible with the fit in some panels, although the TEC rise in that sector
203 can be discerned within the data. The thermosphere-ionosphere coupling effect (double TEC
204 peak shape) is more remarkable during the high solar activity phase. During this phase, the
205 ionosphere is denser due to larger EUV fluxes. This is manifested with a stronger Martian
206 plasma obstacle to compete with the solar wind [e.g. Sánchez-Cano et al., 2016; Hall et al., 2016],
207 and as it is shown in Figure 2, with a more intense coupling between the thermosphere and the
208 ionosphere. Regarding its SZA dependence, the TEC observations show that the coupling in the
209 dayside is stronger and becomes weaker as the nightside approaches (i.e. larger SZA). This
210 coupling is maintained longer into the nightside, up to SZA~105° during the high solar activity
211 phase, while it is only visible up to SZA~90° (day-night terminator) at the low solar activity
212 phase. For larger SZA intervals there is no evidence for this atmospheric coupling in the
213 ionosphere as seen with the TEC, since the TEC is on average almost constant for all Ls. This is
214 expected as the ionosphere is very faint during the nightside [Withers et al., 2012] because the
215 main photoionization source, the solar radiation, is not present. Regarding the time occurrence
216 of both maxima, both are regularly observed at Ls~30°-50° and 210°-230° in all panels in which
217 the coupling is observed. We note that the presence of crustal fields in the southern hemisphere,
218 statistically, do not seem to have any distinguishable effect on these trends. Cartacci et al.
219 [2013] showed that the TEC on the nightside shows a typical increase of 5% over the regions of
220 quasi vertical magnetic fields, and a small decrease of 2% over the regions of quasi horizontal
221 magnetic fields. Although significant, these variations are too small to affect our statistics where
222 data from global coverage and for more than 10 years are averaged. We conclude that the
223 annual occurrence of both TEC maxima are not dependent on solar conditions such as the SZA
224 or the solar activity.

225 4. Ionosphere-Thermosphere Coupling: Polar Latitudes

226 Figure 3 shows the TEC behavior of the polar Regions (latitudes larger than $\pm 85^\circ$). These
227 regions are two of the most sampled areas of the planet by the MARSIS radar, as the polar cap
228 mapping was one of the mission priorities [Orosei et al., 2015]. Consequently, the TEC data
229 coverage of these regions is excellent. As on Earth, SZA and local time parameters do not have a
230 daily key role at these latitudes. However, the main difference with Earth is that the Martian
231 TEC only responds to solar irradiance changes and neutral atmospheric variations at these
232 latitudes because Mars does not have a global internal magnetic field. Another important factor
233 to consider is the heliocentric distance (Figure 1f), which results in different levels of solar
234 irradiance when each pole is illuminated. The TEC maximum of the South pole is 1.3 times
235 larger in magnitude than the North pole TEC maximum (Figures 3a-3b) during the half-year
236 polar dayside, which is coherent with the ratio of heliocentric distances of the perihelion and
237 aphelion. We note that in this figure we have not distinguished between solar activity phases
238 because we did not observe any significant TEC difference with the solar activity. The TEC
239 maximum at the South Pole is centered between the perihelion and the summer solstice
240 ($L_s=251^\circ-270^\circ$), while in the North Pole, it is centered at $L_s=50^\circ-80^\circ$ around aphelion ($L_s=71^\circ$)
241 and just before the summer solstice (similar L_s to the second TEC peak in Figure 1a).

242 During the \sim half-year nightside of each polar cap, the ionosphere is still present although very
243 weak, maintained by processes such as dayside transport or electron precipitation [e.g. Fox et
244 al., 1993]. Figures 3c-3d show the polar night ionosphere of each hemisphere respectively. The
245 dashed line indicates the sensitivity level of MARSIS, as calculated by Mouginot et al. [2008]. To
246 better visualize the averaged TEC values, we have performed two Huber robust fits [Huber,
247 1964], one to all the data that has previously passed the frequency and SNR selection criteria,
248 and another one only to the nightside data above the sensitivity level. If we consider first all the
249 data, the nightside ionosphere of the North Pole is ~ 1.7 times denser on average than both the
250 South Pole nightside ionosphere and the sensitivity level, indicating a weak but present
251 ionosphere during all the half-year nightside. However, the nightside ionosphere of the South
252 Pole is faint, close to the sensitivity level. Considering only data above the sensitivity level, the
253 ratio between the north and south pole nightside ionosphere is equal to 1.3. The MCD estimates
254 that the column density during the North polar winter is 1.9 times larger than during the South
255 polar winter, as calculated for the L_s and latitude conditions of each polar night in Figure 3, for a
256 LT of 18h, and longitude of 180° . Therefore, the measured ratio of the polar night electron
257 densities is also coherent with the changes in the polar night thermospheric densities, as the
258 electron density is proportional to the square root of the neutral density [Chapman, 1931].
259 Additionally, another important process to consider is the day-night plasma transport and polar
260 neutral winds that can have an effect on the level of ionization of each polar night. Since the

261 winter in the North Pole occurs while Mars is transiting its perihelion, plasma transport from
262 the dayside regions of the ionosphere to the polar nightside could be larger than during winter
263 in the South Pole, which occurs at aphelion and when the dayside ionosphere is less robust
264 because less solar irradiance reaches Mars.

265 **5. Ionosphere-Thermosphere Simulation**

266 To evaluate if variations of the neutral atmosphere are responsible for the seasonal TEC
267 variations observed in the MARSIS dataset, we have performed a numerical simulation of the
268 ionosphere during a Martian year. We have used the Mars version of the numerical/physical
269 model IRAP plasmasphere-ionosphere model (IPIM) [Marchaudon and Blelly, 2015], which is an
270 updated version of the TRANSCAR and TRANSMARS family of models [e.g. Blelly et al., 1996;
271 2005; Witasse et al., 2002; Morel et al., 2004; Sánchez-Cano et al., 2015b; Ramirez-Nicolas et al.,
272 2016]. The model is a physical description of the thermosphere and ionosphere of Mars using
273 kinetic and fluid formalisms. The IPIM model can be run from the Transplanet's Space Weather
274 Prediction Center (<http://transplanet.cdpp.eu>), which is a source for planetary space weather
275 forecasts [André et al., 2017]. Moreover, the Mars version of IPIM is coupled with the previously
276 described MCD-LMD atmospheric model (version 5.3), which is used as input for the neutral
277 atmosphere and it is currently one of the most up to date and used models of the atmosphere of
278 Mars. The simulation was performed for one Martian year with SZA=85° and local time 18h in
279 all latitudes (similar conditions to Figure 1a). The main difference is that the solar flux was kept
280 constant, varying only with the heliocentric distance, for the entire simulation to avoid
281 ionospheric variations due to changes in the solar activity that would mask the effect of the
282 neutral atmosphere on the TEC results. The solar flux was fixed for the 8 February 2013
283 (F10.7=104, medium solar activity conditions).

284 Outputs from the simulation are plotted in Figure 4 in the form of contour plots of latitude
285 versus Ls. To produce these plots, outputs were gridded using a Triangulation-based linear
286 interpolation, and only considered latitudes from which simulation outputs could be retrieved.
287 The column density between 100 and 200 km of the major neutral species in Mars'
288 thermosphere are plotted on the right panels, which should be similar to the MCD outputs. At
289 spring and summer in the northern hemisphere (Ls=0°-180°), the simulation shows that there is
290 an increase in the thermospheric O₂, O and N₂ column densities with respect to their respective
291 values along the year, which mainly cover the period Ls~20°-150°. There is also an increase in
292 CO₂ in the northern hemisphere thermosphere, but less significant than for the other molecules.
293 On the other hand, there is a significant reduction of this molecule in the southern polar cap
294 region, which may be related to the CO₂ condensation in the lower atmosphere due to the

295 winter season in the southern hemisphere. At spring and summer in the southern hemisphere
 296 (Ls=180°-270°) something similar occurs, although the chemistry involved is slightly different.
 297 The thermospheric column density of CO₂, O₂, N₂, and H show an increase between Ls~210° and
 298 320° mainly in the southern polar cap which spreads to northern mid-latitudes. These increases
 299 could be related to a warmer and thicker thermosphere (seasonal atmospheric expansion) due
 300 to a closer distance to the Sun.

301 The TEC and the contribution of different ions to the TEC are plotted on the left panels. Due to
 302 electron-neutrality:

$$303 \quad TEC_{electrons} = \sum_{i=1}^n TEC_{ion_i} \quad (1)$$

304 where n is the total number of ion species and i is the count of each one. The simulation shows
 305 that at northern spring (Ls=0°-90°), there is a significant increase in the TEC contribution from
 306 the ions O⁺, O₂⁺ and NO⁺ in both hemispheres, NO⁺ being mainly significant in the southern mid-
 307 latitude hemisphere. On the contrary, there is a significant decrease in the TEC contribution
 308 from the ion CO₂⁺, especially in the southern polar cap which coincides with the CO₂ column
 309 density reduction. Near aphelion and the start of the northern summer (Ls~70°-120°), there is a
 310 large reduction in the N₂⁺, NO⁺ and O₂⁺ TEC contributions, which match with the TEC and
 311 irradiance minima for this period. At spring in the southern hemisphere (Ls=180°-270°), there
 312 is a global CO₂⁺ increase, which coincides with an O₂⁺, N₂⁺ and H⁺ ion increases at the northern
 313 polar cap.

314 Figure 5 shows the contribution in percentage of each ion to the total TEC from the previous
 315 simulation. To get the contribution, each ion value has been divided by the corresponding TEC
 316 value for each Ls bin, and multiplied by 100. Therefore, the annual TEC profile is a straight line
 317 at the 100% level. Three different latitude bands have been plotted, i.e., the North Pole region
 318 (latitudes>60°), the equator region (-10°<latitude<10°), and the South Pole region (latitudes<-
 319 60°). For the three cases, as expected, the largest contribution to the TEC comes from the O₂⁺
 320 ion, which oscillates between the 77 and 82% (tending to be larger at Ls~0°-180°, and lower at
 321 Ls~180°-360°). The second largest contribution comes from the O⁺ and CO₂⁺ ions (3-13%),
 322 which have the opposite behavior during the Martian year, i.e., when one is maximum the other
 323 one is minimum, and viceversa. This is consistent from the chemistry point of view, because O₂⁺,
 324 which is the major ion in the Martian ionosphere, is mainly formed via the reactions:



327 For $L_s \sim 20^\circ - 140^\circ$, the simulation indicates that the O^+ contribution to the TEC is 3-7% larger
328 than that of CO_2^+ for the three latitude bands, having a maximum/minimum respectively at
329 $L_s \sim 45^\circ$. On the other hand, the MCD model estimates that for the same L_s sector, the O column
330 density has a peak 3 times larger than when compared to the last L_s bin of the year (Figure 1d),
331 while the CO_2 column has almost no variation. Consequently, increased levels of atomic oxygen
332 results in more O^+ ions to be produced. Then, the CO_2^+ loses by reaction with atomic oxygen is
333 larger, and this is clearly observed in the CO_2^+ contribution to the TEC. The peak of O_2^+ which
334 leads to the TEC peak is therefore explained by the increase of the 2 major production processes
335 of this ion (equations 2 and 3).

336 For $L_s \sim 140^\circ - 360^\circ$, something different occurs. The main TEC peak (Figure 1a) is obviously
337 formed by the maximum of solar flux (Figure 1e) and by the maximum neutral atmosphere
338 column density (Figures 1 and 4). Considering only the atmospheric effect as in the simulation,
339 the CO_2^+ contribution to the TEC is $\sim 10\%$ larger than the O^+ one, being almost constant from
340 $L_s \sim 215^\circ - 345^\circ$. For this L_s sector, the MCD model estimates that the O column density has
341 almost no variation, while the CO_2 column density has a peak 3 times larger than when
342 compared to the last L_s bin of the year (Figure 1d). Therefore, for this period of the year,
343 increased levels of CO_2 result in more CO_2^+ ions being produced, and as a result, O^+ is reduced.
344 Following equations 2 and 3, the peak of O_2^+ (and so, the TEC) is formed.

345 Regarding other minor, but not negligible species, the simulation indicates that NO^+ and N_2^+
346 contribute to the total TEC, on average, less than 2%. NO^+ dominates over N_2^+ for $L_s < 150^\circ$,
347 having a peak in the three latitudes bands at $L_s = 45^\circ$. This peak is a 3.6% contribution to the TEC
348 at the south polar Regions, a 2.6% at the equator, and a 2.3% at the north polar Regions. For
349 $L_s > 150^\circ$, N_2^+ dominates over NO^+ and its contribution to the TEC is almost a constant below a
350 2% level. Finally, the minor ion for $L_s < 150^\circ$ is H^+ , the contribution to the TEC of which can be
351 considered, on average, negligible. However, for $L_s > 150^\circ$, there is a significant increase of this
352 ion, reaching the order of NO^+ and N_2^+ at the south pole and equator regions, and $\sim 2\%$ larger at
353 the north polar regions.

354 **6. Discussion: Can TEC Be Considered as a Diagnostic Tool for the Coupling Between the** 355 **Lower and Upper Atmosphere?**

356 In this work, we have shown for the first time that the TEC routinely measured by Mars Express
357 is an excellent indicator of the long-term variability of the thermosphere with latitude, SZA,
358 seasons and solar cycle phases. Moreover, it seems that it can also be a good indicator of the
359 dynamics of the coupling between the lower and upper atmosphere. Numerous previous studies
360 have shown different aspects of this coupling, such as planetary and tidal waves that move from

361 the low atmosphere to the thermosphere [e.g. Forbes et al., 2002; Bougher et al., 2001; 2004],
362 gravity waves [e.g. England et al., 2017], northern polar warming of the lower thermosphere
363 near the perihelion/winter solstice [Bougher et al., 2006], the effect of the seasonal thermal
364 expansion/contraction of the Mars lower atmosphere [e.g. Bougher et al., 2004], or the
365 expansion of the entire atmosphere during dust storms [e.g. Keating et al., 1998]. There are
366 other processes that occur in the lower-middle atmosphere, such as atmospheric cycles of
367 different species, which may propagate upwards to the upper atmosphere, although this is a
368 point in which we are still lacking a clear qualitative description.

369 An example is the CO₂ cycle, in which the mass of the atmosphere can vary up to 30% during
370 seasons [e.g. James et al. 1992]. This is a consequence of the CO₂ condensation that every winter
371 occurs at high latitudes, and the subsequent sublimation during the spring and summer seasons.
372 This cycle induces a large semiannual variation in the daily averaged surface pressure all over
373 the planet [e.g. Forget et al., 2007; Martinez et al., 2017] (Figure 1d). Another case related to the
374 CO₂ cycle is the water cycle, in which water vapor is released into the atmosphere from the
375 polar caps during spring and mainly summer when the CO₂ ice layer has disappeared and a
376 water ice layer is exposed to the atmosphere. Then, this water vapor is transported
377 equatorward by the atmosphere [Navarro et al., 2014; Trokhimovskiy et al., 2015], being a
378 factor of 2 smaller during the southern hemisphere spring than during the northern hemisphere
379 spring. During winter, both seasonal CO₂ polar caps act as a sink for any atmospheric water
380 vapor [Harbele et al., 2003]. Moreover, other species like O, O₂, or O₃ have been shown to have
381 also a cyclic behavior during the year, that somehow depend on these polar cap processes. The
382 Mars Express-SPICAM instrument has shown the long-term evolution of these species below
383 50km, which have a maximum of production during the northern spring season [see the review
384 of Montmessin et al., 2017 and references in there]. Specifically, O₃ shows a strong anti-
385 correlation with water vapor, which makes the O₃ column density to be larger at high latitudes
386 during early spring of each hemisphere and totally disappear during the summer seasons [e.g.
387 Perrier et al., 2006].

388 We have shown in Figure 4 that for fixed solar conditions, there is a significant thermospheric
389 increase of O, O₂, N₂ molecules in the most northern latitudes during spring coinciding with the
390 CO₂ sublimation period of the Northern polar cap (Ls=0-70°). The increase of these neutral
391 species result in more N₂⁺, O₂⁺, O⁺, NO⁺ ions in the ionosphere at all latitudes during this time of
392 the Martian year, and therefore, in a significant TEC increase. This thermospheric variability,
393 that is repeated every Martian year independently of the solar activity levels, is likely linked to
394 atmospheric variability produced by cycles at lower atmospheric levels. Our results seem to be
395 supported by the Mars Express-SPICAM observations of the lower atmosphere. Thermospheric

396 O₂ column densities have similar increases both in latitude and Ls with respect to O₂ column
397 density observations of the low-mid atmosphere (e.g. see Montmessin et al., 2017, Figure 1),
398 being maximum in the early northern and southern springs in both hemispheres. As a
399 consequence, the double peak in the TEC as a function of a Martian year could be the result of a
400 larger increase in the column density of oxygen species, caused by the semiannual atmospheric
401 cycles produced by the sublimation of the polar caps.

402 There are other seasonal factors that have been proved to have an effect on the thermosphere-
403 ionosphere system. For example, there are typically large amounts of dust suspended in the
404 lower atmosphere during the dust season (near the perihelion) that have a heating effect on the
405 lower atmosphere [e.g. Bougher et al., 2001; Wang and Nielsen et al., 2003; Withers et al., 2009].
406 This produces a thermal expansion of the lower atmosphere that is also observed in the upper
407 atmosphere, and as a consequence, produces an increase in the altitude of the ionospheric peak
408 [e.g. Hantsch and Bauer, 1990]. Furthermore, Withers et al. [2015] recently re-analyzed the
409 Mariner 9 radio-occultation profiles that were recorded during a severe global dust storm
410 [Kliore et al., 1972] and found a similar result, the ionosphere was systematically lifted upward
411 by 20-30 km, although, the peak density of the ionosphere was not affected. These observations
412 suggest that while the ionosphere/thermosphere system was only moved upward, the total
413 electron/ion column density, the TEC, was not affected. In our case, since the TEC peak observed
414 in Figure 1a occurred before aphelion (not in the dust storm season) and is always observed at
415 different latitudes, dayside and solar cycle phases, we do not expect it to be a consequence of
416 any of the above mentioned factors which lead to a lift of the atmosphere. Instead, as data and
417 modelling suggest, the low-upper atmospheric coupling due to atmospheric cycles seems more
418 plausible.

419

420

421 **7. Conclusions**

422 In this paper, we have shown for the first time that the total electron content (TEC) of the
423 ionosphere is an interesting indicator of the dynamic of the thermosphere-ionosphere coupling,
424 and can be used as a tracer for the variability of the thermosphere. Using 10 years of MEX TEC
425 observations we have assessed the seasonal, latitudinal and solar cycle variability of this
426 coupling. The annual TEC profile closely follows the irradiance profile with a maximum near
427 perihelion and a minimum near aphelion because, the solar flux is the dominant factor for
428 ionization as expected. However, the TEC annual profile shows an unexpected secondary

429 maximum at $L_s=25^\circ-75^\circ$, which is not related to the annual irradiance variation. This is
430 observed during the northern spring season and before aphelion, and occurs together with an
431 increase in both the thermospheric density and the surface pressure. These double peaks in the
432 annual TEC profile occur always at the same L_s , and are most likely a consequence of the
433 seasonal variability of the thermosphere.

434 Moreover, we have performed a numerical simulation of the ionosphere-thermosphere of Mars
435 with the IPIM model for a Martian year, under the constraint that the solar flux was kept
436 constant for the full simulation, varying only with the heliocentric distance. The results show
437 that the ion contribution to the TEC vary with season, being O^+ more important than CO_2^+ during
438 the first part of the year (northern spring and summer) at all latitudes, and CO_2^+ more important
439 than O^+ during the second part of the year (northern autumn and winter). On average, both ion
440 species have an equal contribution to the TEC at each half of the year. Seasonal change of these
441 ions may be related to the lower atmosphere cycles, which produce a large semiannual mass
442 atmospheric change with seasons. We show that this large amount of atmospheric mass
443 variability could have a significant effect on the thermosphere, and therefore, on the ionosphere,
444 especially near the aphelion of the Mars' orbit when the sublimation of the northern polar cap
445 occurs and the solar irradiance is near the lowest value.

446 In conclusion, the TEC parameter which is routinely measured by Mars Express since mid-2005,
447 seems to be a promising tracer for the dynamic of the thermosphere-ionosphere coupling at
448 least on the dayside region near terminator as supported by numerical simulations. Moreover, it
449 seems to be a reliable indicator of the state of the lower-upper atmospheric coupling.

450 **Acknowledgments**

451 B.S.-C. and M.L. acknowledge support through STFC grant ST/N000749/1. ESA-ESTEC Faculty
452 and Europlanet funding are also gratefully acknowledged. MEX MARSIS RDR and EDR data can
453 be downloaded from the ESA-PSA archive, TIMED-SEE data at the University of Colorado's
454 website (<http://lasp.colorado.edu/lisird/index.html>), REMS data at the NASA Planetary Data
455 System (http://atmos.nmsu.edu/PDS/data/mslrem_1001/DATA/), the MCD model at the Mars
456 Climate Database web interface (<http://www-mars.lmd.jussieu.fr/mars/access.html>), and the
457 IPIM model at the IRAP CDPP web interface (<http://transplanet.irap.omp.eu/>).

458

459 **References**

- 460 – André et al., 2017, Virtual Planetary Space Weather Services offered by the Europlanet H2020
461 Research Infrastructure, Planetary and Space Science, 150, 50-59,
462 <https://doi.org/10.1016/j.pss.2017.04.020>
463
- 464 – Blelly, P.-L., Lilensten, J., Robineau, A., Fontanari, J., and Alcaydé, D. (1996), Calibration of a
465 numerical ionospheric model with EISCAT observations, *Ann. Geophys.*, 14, 1375–1390
466
- 467 – Blelly, P. L., C. Lathuillère, B. Emery, J. Lilensten, J. Fontanari, and D. Alcaydé, (2005), An
468 extended TRANSCAR model including ionospheric convection: simulation of EISCAT
469 observations using inputs from AMIE, *Ann. Geophys.*, 23, 419-431,
470 <https://doi.org/10.5194/angeo-23-419-2005>
471
- 472 – Bougher, S. W., S. Engel, D. P. Hinson, and J. M. Forbes (2001), Mars Global Surveyor Radio
473 Science electron density profiles: Neutral atmosphere implications, *Geophys. Res. Lett.*, 28,
474 3091–3094.
475
- 476 – Bougher, S. W., S. Engel, D. Hinson, and J. Murphy (2004), MGS radio science electron density
477 profiles: Interannual variability and implications for the Martian neutral atmosphere, *J.*
478 *Geophys. Res.*, 109, E03010, [doi:10.1029/2003JE002154](https://doi.org/10.1029/2003JE002154).
479
- 480 – Bougher, S. W., J. M. Bell, J. R. Murphy, M. A. Lopez-Valverde, and P. G. Withers (2006), Polar
481 warming in the Mars thermosphere: Seasonal variations owing to changing insolation and dust
482 distributions, *Geophys. Res. Lett.*, 33, L02203, [doi:10.1029/2005GL024059](https://doi.org/10.1029/2005GL024059).
483
- 484 – Bougher, S. W., T. E. Cravens, J. Grebowksy, and J. Luhmann (2015), The aeronomy of Mars:
485 Characterization by MAVEN of the upper atmosphere reservoir that regulates volatile escape,
486 *Space Sci. Rev.*, 195, 423–456, [doi:10.1007/s11214-014-0053-7](https://doi.org/10.1007/s11214-014-0053-7).
487
- 488 – Bougher, S. W., et al. (2017), The structure and variability of Mars dayside thermosphere from
489 MAVEN NGIMS and IUVS measurements: Seasonal and solar activity trends in scale heights
490 and temperatures, *J. Geophys. Res. Space Physics*, 122, [doi:10.1002/2016JA023454](https://doi.org/10.1002/2016JA023454).
491
- 492 – Cartacci, M., Amata, E., Cicchetti, A., Noschese, R., Giuppi, S., Langlais, B., Frigeri, A., Orosei, R.,
493 Picardi, G., 2013. Mars ionosphere total electron content analysis from MARSIS subsurface
494 data. *Icarus*, 223, 423–437. <http://dx.doi.org/10.1016/j.icarus.2012.12.011>.
495

- 496 – Cartacci, M., B. Sánchez-Cano, R. Orosei, R. Noschese, A. Cicchetti, O. Witasse, F. Cantini, A. Pio
497 Rossi, (2018), Improved estimation of Mars ionosphere total electron content, *Icarus*, 299,
498 396-410, <https://doi.org/10.1016/j.icarus.2017>
499
- 500 – Chapman, S. and Bartels, J. (1940) *Geomagnetism*. Oxford University Press, Oxford, 1049 p.
501
- 502 – Chapman, S. (1931), Absorption and dissociative or ionizing effects of monochromatic
503 radiation in an atmosphere on a rotating earth, *Proc. Phys. Soc. Lond.*, 43, 26–45.
504
- 505 – Chicarro, A., Martin, P., Trautner, R., (2004). The Mars Express mission: an overview. In:
506 Wilson, A., Chicarro, A. (Eds.), *Mars Express: The Scientific Payload* vol. 1240. ESA Special
507 Publication, Noordwijk, The Netherlands, pp.3–13.
508
- 509 – England, S. L., G. Liu, E. Yiğit, P. R. Mahaffy, M. Elrod, M. Benna, H. Nakagawa, N. Terada, and B.
510 Jakosky (2017), MAVEN NGIMS observations of atmospheric gravity waves in the Martian
511 thermosphere, *J. Geophys. Res. Space Physics*, 122, 2310–2335, [doi:10.1002/2016JA023475](https://doi.org/10.1002/2016JA023475).
512
- 513 – Forbes, J. M., A. F. C. Bridger, M. E. Hagan, S. W. Bougher, J. L. Hollingsworth, G. M. Keating, and
514 J. R. Murphy (2002), Nonmigrating tides in the thermosphere of Mars, *J. Geophys. Res.*,
515 107(E11), 5113, [doi:10.1029/2001JE001582](https://doi.org/10.1029/2001JE001582).
516
- 517 – Forget, F., F. Hourdin, O. Talagrand, (1998), CO₂ snow fall on Mars: Simulation with a general
518 circulation model, *Icarus*, 131, 302–316.
519
- 520 – Forget, F., F. Hourdin, R. Fournier, C. Hourdin, O. Talagrand, M. Collins, S. R. Lewis, P. L. Read, J-
521 P. Huot, (1999), Improved general circulation models of the Martian atmosphere from the
522 surface to above 80 km, *J. Geophys. Res.*, 104, 24,155–24,175
523
- 524 – Forget, F., A. Spiga, B. Dolla, S. Vinatier, R. Melchiorri, P. Drossart, A. Gendrin, J.-P. Bibring, Y.
525 Langevin, and B. Gondet (2007), Remote sensing of surface pressure on Mars with the Mars
526 Express/OMEGA spectrometer: 1. Retrieval method, *J. Geophys. Res.*, 112, E08S15,
527 [doi:10.1029/2006JE002871](https://doi.org/10.1029/2006JE002871).
528
- 529 – Fox, J. L., J. F. Brannon, H. S. Porter, (1993), Upper limits to the nightside ionosphere of Mars,
530 *Geophys. Res. Lett.*, 20, 1391–1394
531

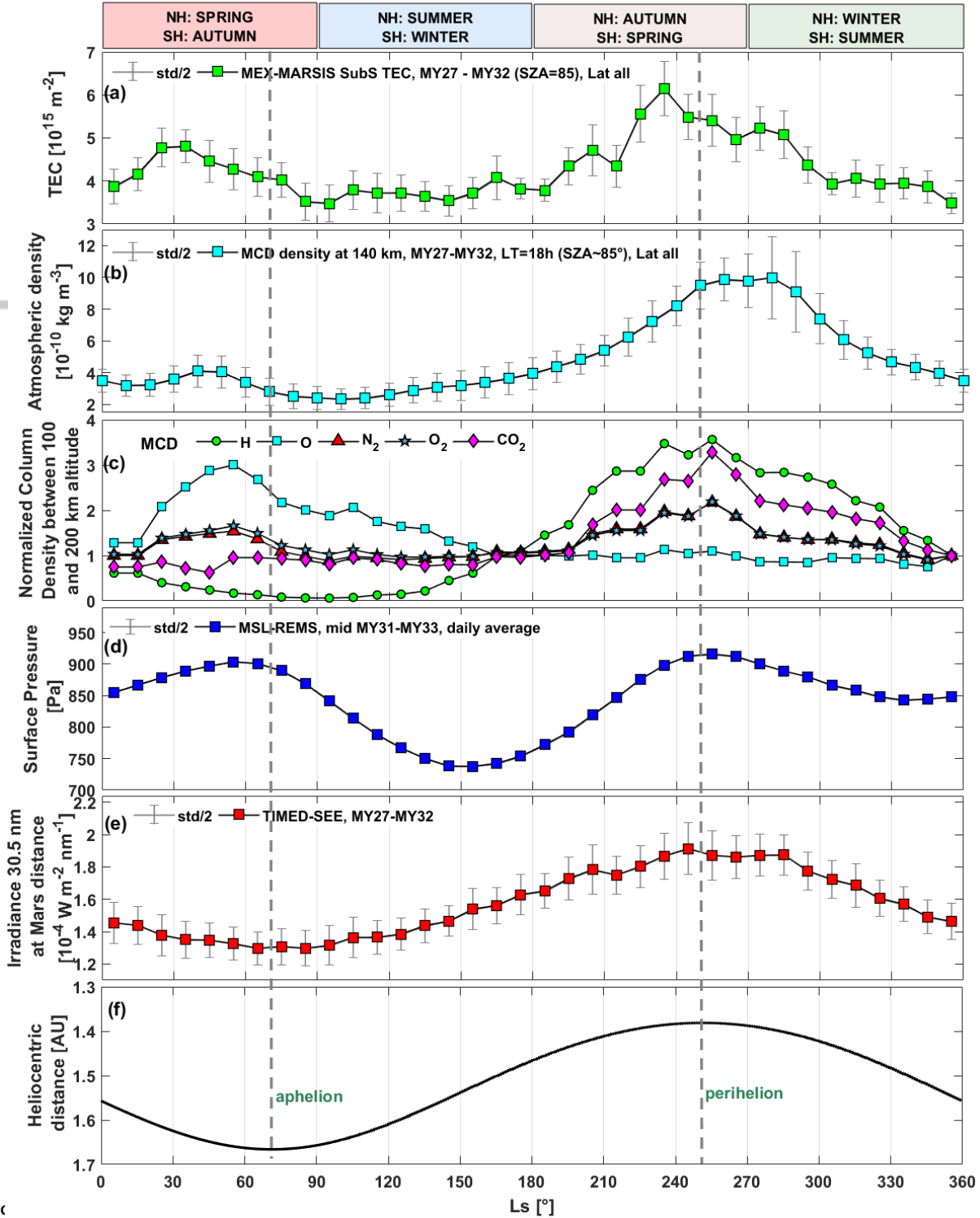
- 532 – Gómez-Elvira, J., et al. (2012), REMS: The environmental sensor suite for the Mars Science
533 Laboratory rover, *Space Sci. Rev.*, 170, 583–640, doi:10.1007/s11214-012-9921-1.
534
- 535 – González-Galindo, F., F. Forget, M. Angelats I Coll, and M. A. López-Valverde (2008). The
536 Martian upper atmosphere. *Lecture Notes and Essays in Astrophysics*, 3:151-162.
537
- 538 – Grotzinger, J. P., et al. (2012), Mars Science Laboratory mission and science investigation,
539 *Space Sci. Rev.*, 170, 5–56, doi:10.1007/s11214-012-9892-2
540
- 541 – Hall, B. E. S., M. Lester, B. Sánchez-Cano, J. D. Nichols, D. J. Andrews, N. J. T. Edberg, H. J.
542 Opgenoorth, M. Fränz, M. Holmström, R. Ramstad, O. Witasse, M. Cartacci, A. Cicchetti, R.
543 Noschese, and R. Orosei, (2016), Annual variations in the Martian bow shock location as
544 observed by the Mars Express mission, *J. Geophys. Res. Space Physics*, 121,
545 doi:10.1002/2016JA023316
546
- 547 – Hantsch, M.H., and S.J. Bauer, (1990), Solar control of the Mars ionosphere, *Planet. Space Sci.*,
548 38, pp. 539-542
549
- 550 – Harbele, R.M., (2003), Planetary atmospheres: Mars, in *The Encyclopedia of Atmospheric*
551 *Science*, Academic Press, pp. 1745-1755. ISBN: 978-0-12-227090-1
552
- 553 – Huber, P. J. (1964). “Robust Estimation of a Location Parameter.” *Annals of Mathematical*
554 *Statistics* 35:73-101
555
- 556 – James, P.B., H.H. Kieffer, and D.A. Paige (1992), The seasonal cycle of carbon dioxide on Mars,
557 in *Mars*, pp. 934–968, The Univ. of Ariz. Press, Tucson.
558
- 559 – Jakosky, (2015), MAVEN explores the Martian upper atmosphere, *Science*, 350, 6261, 643,
560 10.1126/science.aad3443
561
- 562 – Keating, G. M., *et al.* (1998), The structure of the upper atmosphere of Mars: In-situ
563 accelerometer measurements from Mars Global Surveyor, *Science*, 279, 1672–1676.
564
- 565 – Kliore, A.J., D.L. Cain, G. Fjeldbo, B.L. Seidel, S.I. Rasool, (1972), Mariner 9 S-band Martian
566 occultation experiment: Initial results on the topography and atmosphere of Mars, *Science*,
567 175, pp. 313-317
568

- 569 – Lillis, R. J., D. A. Brain, S. L. England, P. Withers, M. O. Fillingim, and A. Safaeinili (2010), Total
570 electron content in the Mars ionosphere: Temporal studies and dependence on solar EUV flux,
571 J. Geophys. Res., 115, A11314, doi:10.1029/2010JA015698.
- 572
- 573 – Madeleine, J.-B., F. Forget, E. Millour, T. Navarro, and A. Spiga (2012), The influence of
574 radiatively active water ice clouds on the Martian climate, Geophys. Res. Lett., 39, L23202,
575 doi:10.1029/2012GL053564.
- 576
- 577 – Marchaudon, A., and P.-L. Blelly, A new 16-moment interhemispheric model of the ionosphere
578 : IPIM, J. Geophys. Res., 120, doi:10.1002/2015JA021193, 2015.
- 579
- 580 – Martínez, G. M., C. N. Newman, A. De Vicente-Retortillo, E. Fischer, N. O. Renno, M. I.
581 Richardson, A. G. Fairén, M. Genzer, S. D. Guzewich, R. M. Haberle, A.-M. Harri, O. Kempainen,
582 M. T. Lemmon, M. D. Smith, M. de la Torre-Juárez, A. R. Vasavada (2017). The modern near-
583 surface Martian climate: A review of in-situ meteorological data from Viking to Curiosity.
584 Space Science Reviews, 212(1-2), 295-338.
- 585
- 586 – Mendillo, M., A. G. Marusiak, P. Withers, D. Morgan, and D. Gurnett (2013), A new
587 semiempirical model of the peak electron density of the Martian ionosphere, Geophys. Res.
588 Lett., 40, 5361–5365, doi:10.1002/2013GL057631
- 589
- 590 – Mendillo, M., C. Narvaez, M. Matta, M. Vogt, P. Mahaffy, M. Benna, and B. Jakosky (2015),
591 MAVEN and the Mars Initial Reference Ionosphere model, Geophys. Res. Lett., 42, doi:10.1002/
592 2015GL065732.
- 593
- 594 – Mendillo, M., et al. (2017a), MAVEN and the total electron content of the Martian ionosphere, J.
595 Geophys. Res. Space Physics, 122, 3526-3537, doi:10.1002/2016JA023474.
- 596 – Mendillo, M., Narvaez, C., & Campbell, B. (2017b). The total electron content of the Martian
597 ionosphere from MRO/SHARAD observations. Journal of Geophysical Research: Planets, 122,
598 2182–2192. <https://doi.org/10.1002/2017JE005391>
- 599 – Millour, E., et al. (2015), The Mars Climate Database (MCD version 5.2), in European Planetary
600 Science Congress 2015, vol. 10, EPSC2015-438, Nantes, France, 27 Sept.–2 Oct.
- 601
- 602 – Montmessin, F., O. Korablev, F. Lefèvre, J.-L. Bertaux, A. Fedorova, A. Trokhimovskiy, J. Y.
603 Chaufray, G. Lacombe, A. Reberac, L. Maltagliati, Y. Willame, S. Guslyakova, J.-C. Gérard,

- 604 A. Stiepen, D. Fussen, N. Mateshvili, A. Määttänen, F. Forget, O. Witasse, F. Leblanc, A. C.
605 Vandaele, E. Marcq, B. Sandel, B. Gondet, N. Schneider, M. Chaffin, and N. Chapron (2017).
606 SPICAM on Mars Express: A 10 year in-depth survey of the Martian atmosphere. *Icarus*,
607 297:195-216, doi: 10.1016/j.icarus.2017.06.022
608
- 609 – Morel, L., O. Witasse, R. Warnant, J.-C. Cerisier, P.-L. Blelly, and J. Lilensten (2004), Diagnostic
610 of the dayside ionosphere of Mars using the total electron content measurement by the
611 NEIGE/Netlander experiment: An assessment study, *Planet. Space Sci.*, 52(7), 603–611,
612 doi:10.1016/j.pss.2003.12.007.
613
- 614 – Mouginot, J., W. Kofman, A. Safaeinili, and A. Herique (2008), Correction of the ionospheric
615 distortion on the MARSIS surface sounding echoes, *Planet. Space Sci.*, 56, 917–926,
616 doi:10.1016/j.pss.2008.01.010.
617
- 618 – Navarro, T., J.-B. Madeleine, F. Forget, A. Spiga, E. Millour, F. Montmessin, and A. Maattanen
619 (2014), Global climate modeling of the Martian water cycle with improved microphysics and
620 radiatively active water ice clouds, *J. Geophys. Res. Planets*, 119, doi:10.1002/2013JE004550.
621
- 622 – Orosei, R., et al. (2015), Mars Advanced Radar for Subsurface and Ionospheric Sounding
623 (MARSIS) after nine years of operation: A summary, *Planet. Space Sci.*, 112, 98–114,
624 doi:10.1016/j.pss.2014.07.010.
625
- 626 – Perrier, S., J. L. Bertaux, F. Lefevre, S. Lebonnois, O. Korablev, A. Fedorova, and F. Montmessin
627 (2006), Global distribution of total ozone on Mars from SPICAM/MEX UV measurements, *J.*
628 *Geophys. Res.*, 111, E09S06, doi:10.1029/2006JE002681.
629
- 630 – Picardi, G., Biccari, D., Seu, R., Plaut, J., Johnson, W. T. K., Jordan, R. L., Safaeinili, A., Gurnett, D.
631 A., Huff, R., Orosei, R., Bombaci, O., Calabrese, D., Zampolini, E., (2004). MARSIS: Mars advanced
632 radar for subsurface and ionosphere sounding. In: Wilson, A., Chicarro, A. (Eds.), *Mars Express:*
633 *The Scientific Payload vol. 1240.* ESA Special Publication, Noordwijk, The Netherlands, pp.51–
634 69.
635
- 636 – Ramírez-Nicolás, B. Sánchez-Cano, O. Witasse, P.-L. Blelly, L. Vázquez, M. Lester, (2016). The
637 effect of the induced magnetic field on the electron density vertical profile of the Mars'
638 ionosphere: a Mars Express MARSIS radar data analysis and interpretation, a case study,
639 *Planetary and Space Science*, 126, 49–62, doi:10.1016/j.pss.2016.03.017

- 640 – Safaenili, A., Kofman, W., Mouginot, J., Gim, Y., Herique, A., Ivanov, A.B., Plaut, J.J., Picardi, G.,
641 2007. Estimation of the total electron content of the Martian ionosphere using radar sounder
642 surface echoes. *Geophys. Res. Lett.* 34, 23204. <http://dx.doi.org/10.1029/2007GL032154>
- 643 – Sanchez-Cano, B., D.D. Morgan, O. Witasse, S.M. Radicella, M. Herraiz, R. Orosei, M. Cartacci, A.
644 Cicchetti, R. Noschese, W. Kofman, C. Grima, J. Mouginot, D.A. Gurnett, M. Lester, P.-L. Blelly, H.
645 Opgenoorth, G. Quinsac, (2015a). Total Electron Content in the Martian atmosphere: A critical
646 assessment of the Mars Express MARSIS data sets. *J. Geophys. Res. Space Physics*, 120, 2166–
647 2182, doi:10.1002/2014JA020630
- 648
- 649 – Sánchez – Cano, B., M. Lester, O. Witasse, S.E. Milan, B.E.S. Hall, P.-L. Blelly, S.M. Radicella, D.D.
650 Morgan, (2015b). Evidence of scale height variations in the Martian ionosphere over the solar
651 cycle, *J. Geophys. Res. Space Physics*, 120, 10.913–10.925, doi: 10.1002/2015JA021949
- 652
- 653 – Sánchez-Cano, B., M. Lester, O. Witasse, S.E. Milan, B.E.S. Hall, M. Cartacci, K. Peter, D.D.
654 Morgan, P.-L. Blelly, S. Radicella, A. Cicchetti, R. Noschese, R. Orosei, M. Pätzold, (2016). Solar
655 cycle variations in the ionosphere of Mars as seen by multiple Mars Express datasets, *J.*
656 *Geophys. Res. Space Physics*, 121, doi: 10.1002/2015JA022281
- 657
- 658 – Trokhimovskiy, A., A. Fedorova, O. Korablev, F. Montmessin, J.-L. Bertaux, A. Rodin, M.D. Smith,
659 (2015), Mars' water vapor mapping by the SPICAM IR spectrometer: five Martian years of
660 observations, *Icarus*, 251, 50-64, <https://doi.org/10.1016/j.icarus.2014.10.007>
- 661
- 662 – Wang, J.-S., and E. Nielsen, (2003), Behavior of the Martian dayside electron density peak
663 during global dust storms, *Planetary and Space Science*, Volume 51, Issue 4-5, p. 329-338, doi:
664 10.1016/S0032-0633(03)00015-1
- 665
- 666 – Witasse, O., et al. (2002), Prediction of a CO₂+ layer in the atmosphere of Mars, *Geophys. Res.*
667 *Lett.*, 29(8), 1263, doi:10.1029/2002GL014781.
- 668
- 669 – Witasse, O., T. Cravens, M. Mendillo, J. Moses, A. Kliore, F. Nagy, and T. Breus (2008), Solar
670 system ionospheres, *Space Sci. Rev.*, 139, 235–265, doi:10.1007/s11214-008-9395-3.
- 671
- 672 – Withers, P (2009) A review of observed variability in the dayside ionosphere of Mars. *Adv*
673 *Space Res* 44: 277–307. doi:10.1016/j.asr.2009.04.027.
- 674

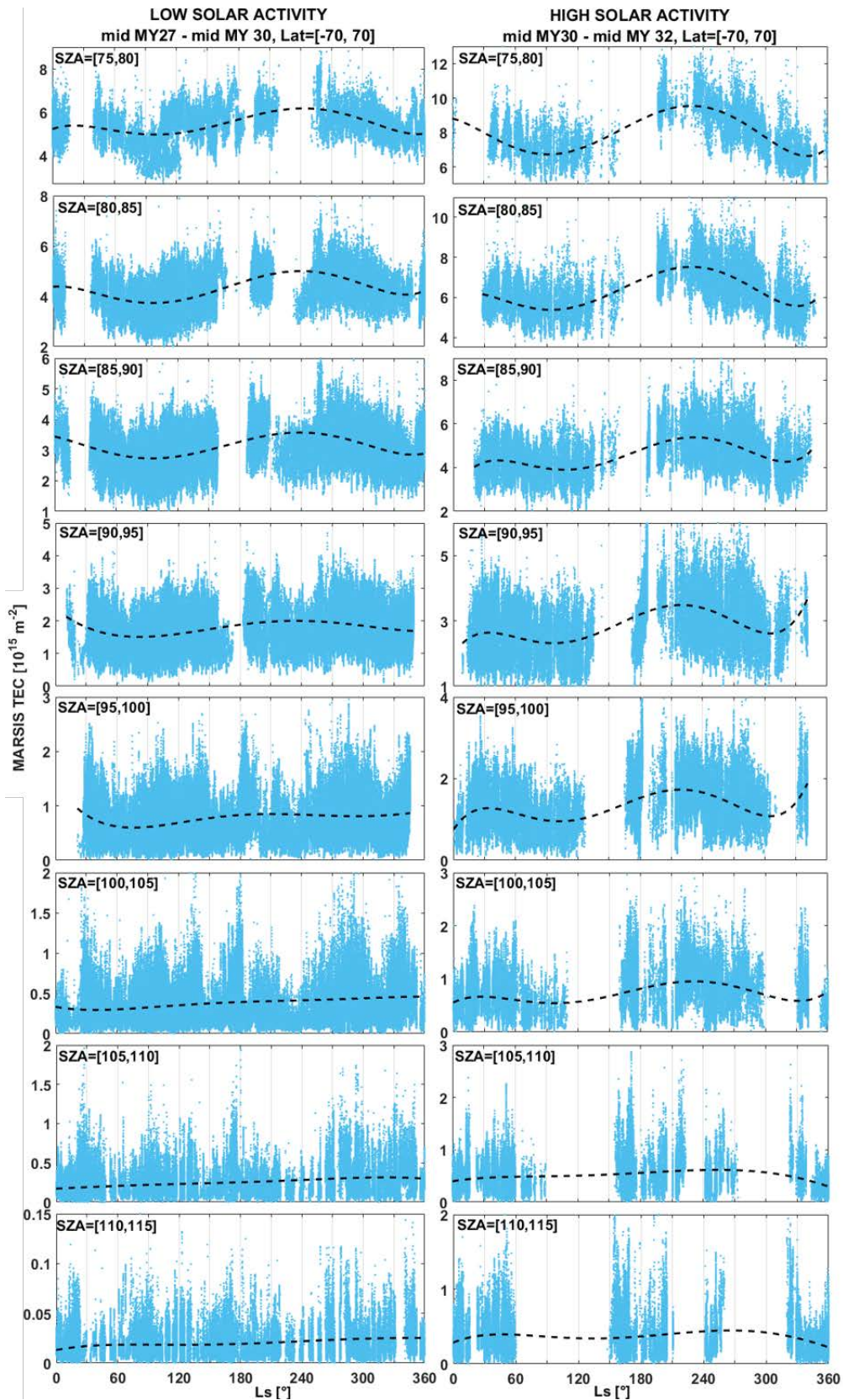
- 675 – Withers, P., Fillingim, M.O., Lillis, R.J., Häusler, B., Hinson, D.P., Tyler, G.L., Pätzold, M., Peter, K.,
676 Tellmann, S., Witasse, O., (2012). Observations of the nightside ionosphere of Mars by the Mars
677 Express Radio Science Experiment (MaRS). *J. Geophys. Res.*, 117, A12307.
678 doi:10.1029/2012JA018185
- 679
- 680 – Withers, P., S. Weiner, and N. R. Ferreri (2015), Recovery and validation of Mars ionospheric
681 electron density profiles from Mariner 9, *Earth Planets Space*, 67(1), 194, doi:10.1186/s40623-
682 015-0364-2.
- 683
- 684 – Woods, T. N., and F. G. Eparvier (2006), Solar ultraviolet variability during the TIMED mission,
685 *Adv. Space Res.*, 37, 219–224, doi:10.1016/j.asr.2004.10.006.
- 686
- 687 – Yigit, E., P. Koucka, K. Georgieva, and W. Ward (2016), A review of vertical coupling in the
688 atmosphere-ionosphere system: Effects of waves, sudden stratospheric warmings, space
689 weather, and of solar activity, *J. Atmos. Sol. Terr. Phys.*, 141, 1–12,
690 doi:10.1016/j.jastp.2016.02.011.
- 691
- 692 – Zurek, R. W., R. A. Tolson, S. W. Bougher, R. A. Lugo, D. T. Baird, J. M. Bell, and B. M. Jakosky
693 (2017), Mars thermosphere as seen in MAVEN accelerometer data, *J. Geophys. Res. Space
694 Physics*, 122, 3798-3814, doi:10.1002/2016JA023641.
- 695
- 696
- 697
- 698



699

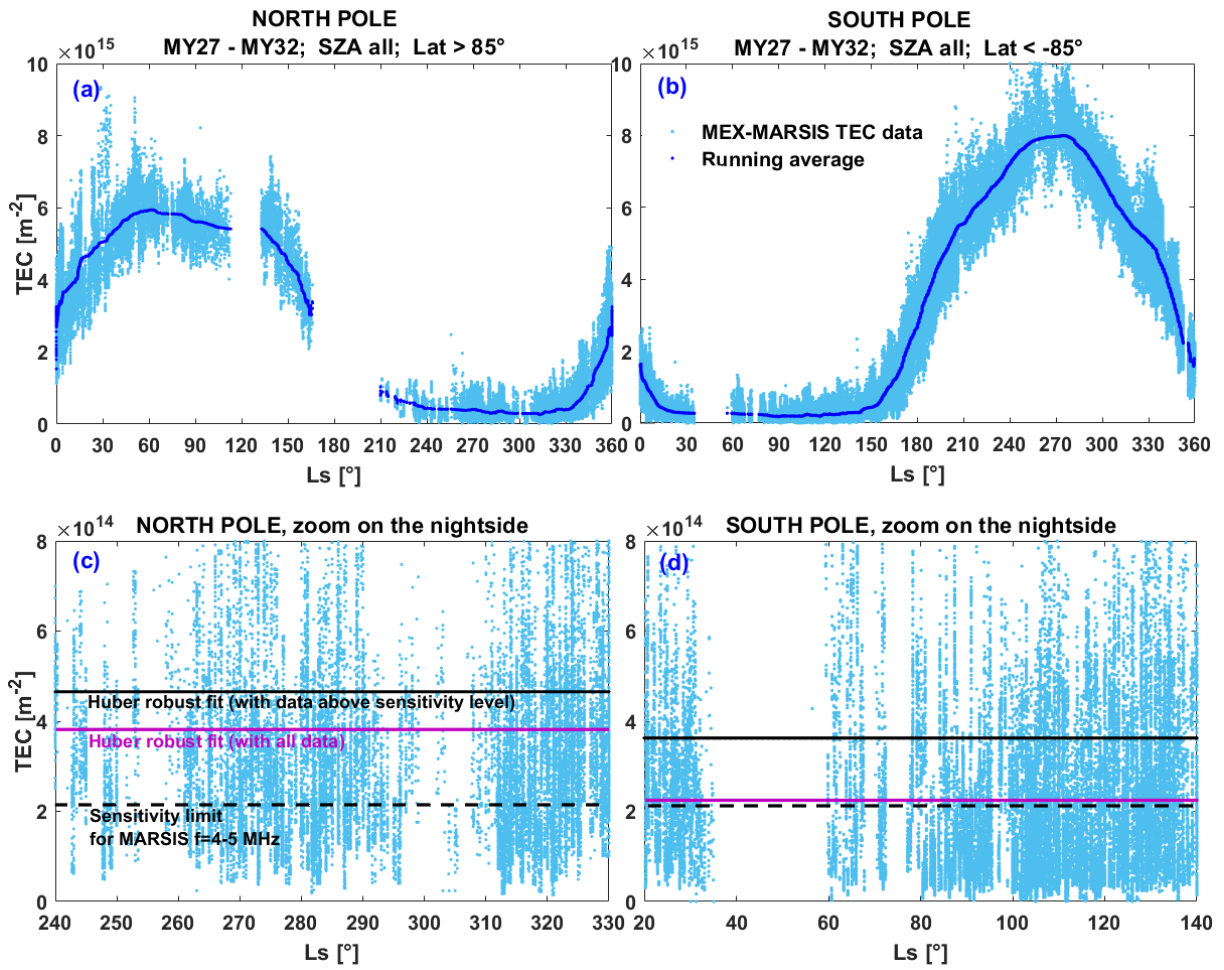
700 **FIGURE 1:** General annual observations. Each parameter in this figure has been averaged within
 701 Ls bins of 10° (squares). The half standard deviation of each Ls bins is shown with a grey
 702 vertical line. Mars' aphelion and perihelion are indicated with two vertical grey dashed lines.
 703 Northern hemisphere (NH) and Southern hemisphere (SH) seasons are indicated at the top of
 704 the figure. (a) MEX MARSIS-TEC of MY 27-32 averaged over all latitudes and for SZA=85°. (b)
 705 Averaged atmospheric density obtained from the MCD at 140km for MY27-32 and all latitudes.

706 Data in this panel varies according the solar flux of each day (c) Temporal variability of the
707 averaged MCD column density between 100-200 km and latitude for the major neutral species,
708 and normalized to their relevant value at $L_s=355^\circ$ (see Figure 4). Data in this panel varies with a
709 constant solar flux that is shaped only by the heliocentric distance (d) MSL-REMS surface
710 pressure average of mid MY 31- 33. (e) TIMED-SEE solar irradiance for the 30.5nm wavelength
711 extrapolated to Mars' distance from MY 27-32. (f) Mars' heliocentric distance.



712

713 **Figure 2:** (Left) TEC of low solar activity period for increasing SZA. (Right) Same, for the high
 714 solar activity period. The dashed lines correspond to the best fit to the data.



715

716

FIGURE 3: Annual TEC of the polar ionosphere. (a) North Pole. (b) South Pole. (c) Zoom on the North Pole nightside. (d) Zoom on the South Pole nightside.

717

718

719

720

721

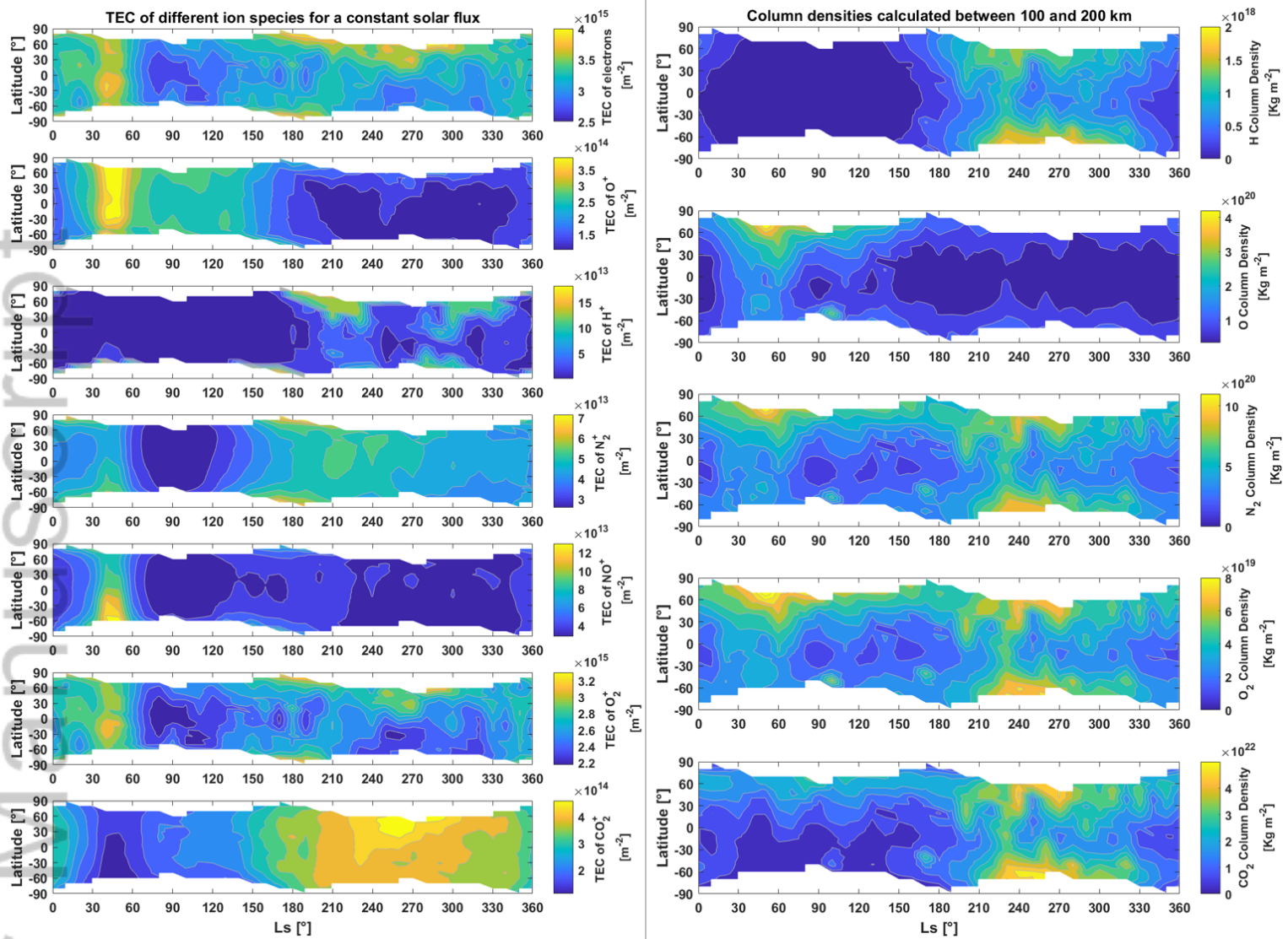
722

723

724

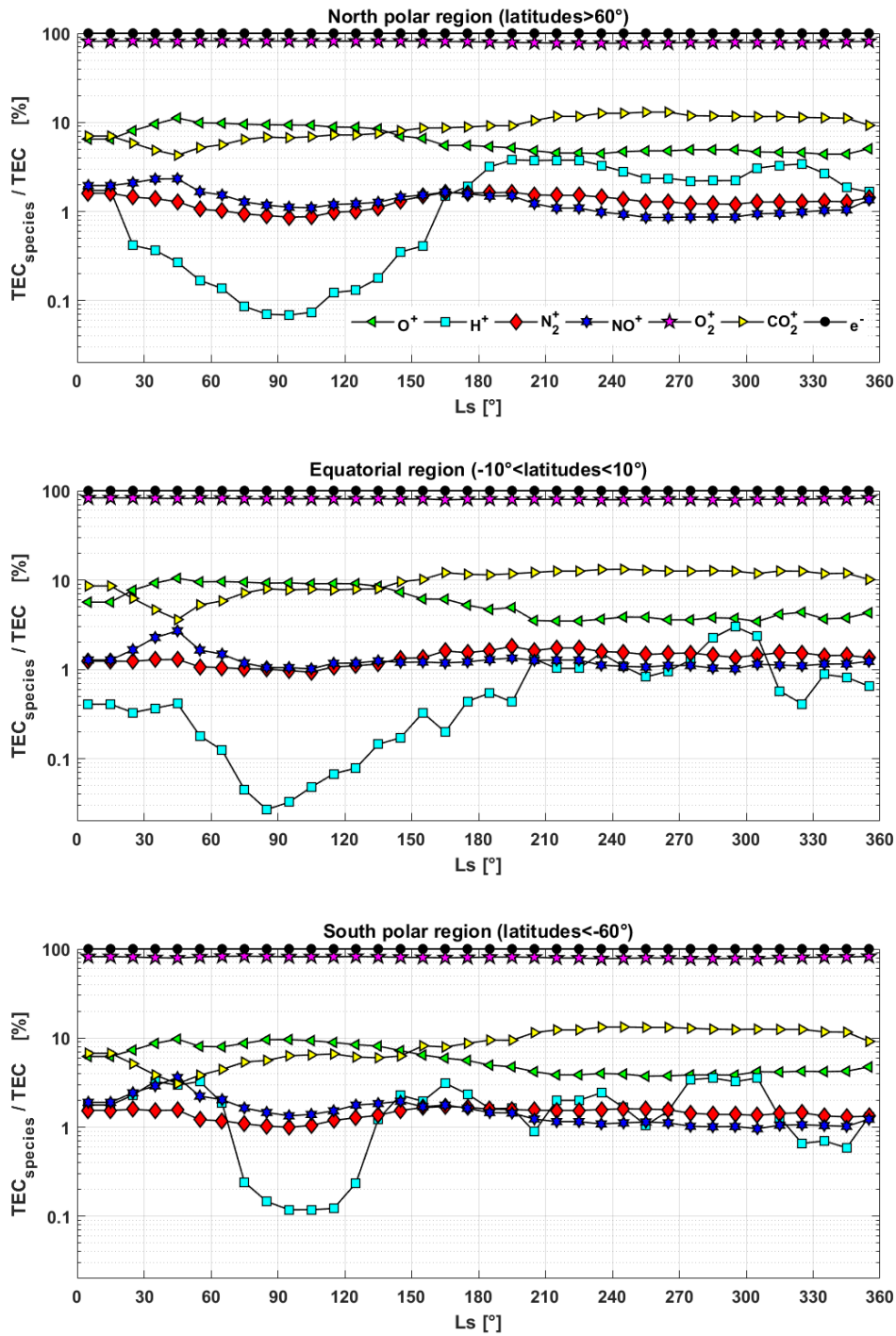
725

726



728 **Figure 4:** IPIM ionospheric simulations for SZA=85°, local time 18h, and a constant solar flux
 729 fixed for the day 8 February 2013. The IPIM model is coupled with the GCM-LMD model, whose
 730 outputs come from the Mars Climate Dataset (MCD) 5.3 version. All the panels show the latitude
 731 evolution of the following parameters in a Martian year (via proxy Ls). (Left panels) TEC
 732 contribution of each of the main ion species. (Right panels) Column density between 100 and
 733 200 km of each major neutral species. Note the different scale of the colorbars.

734



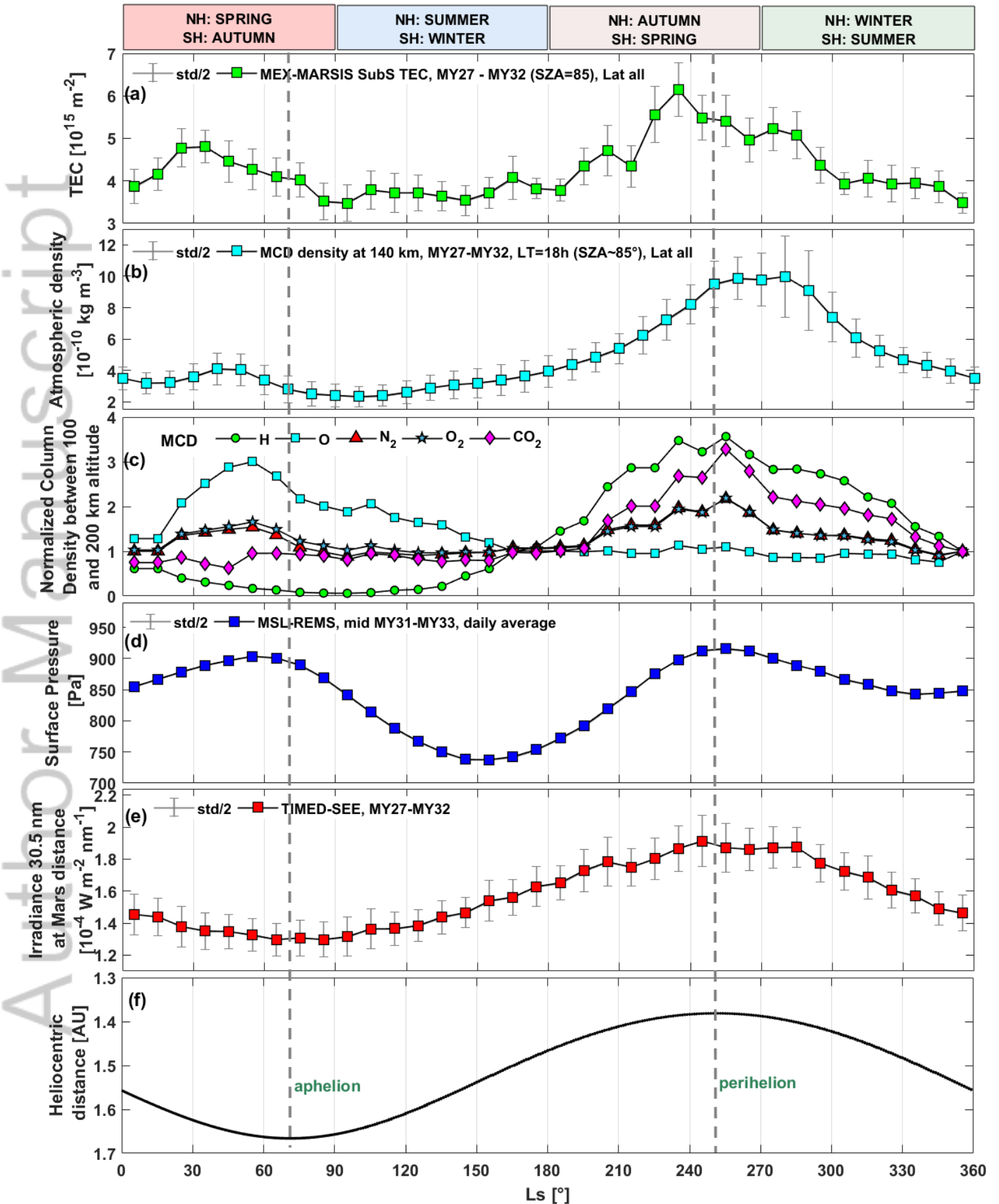
735

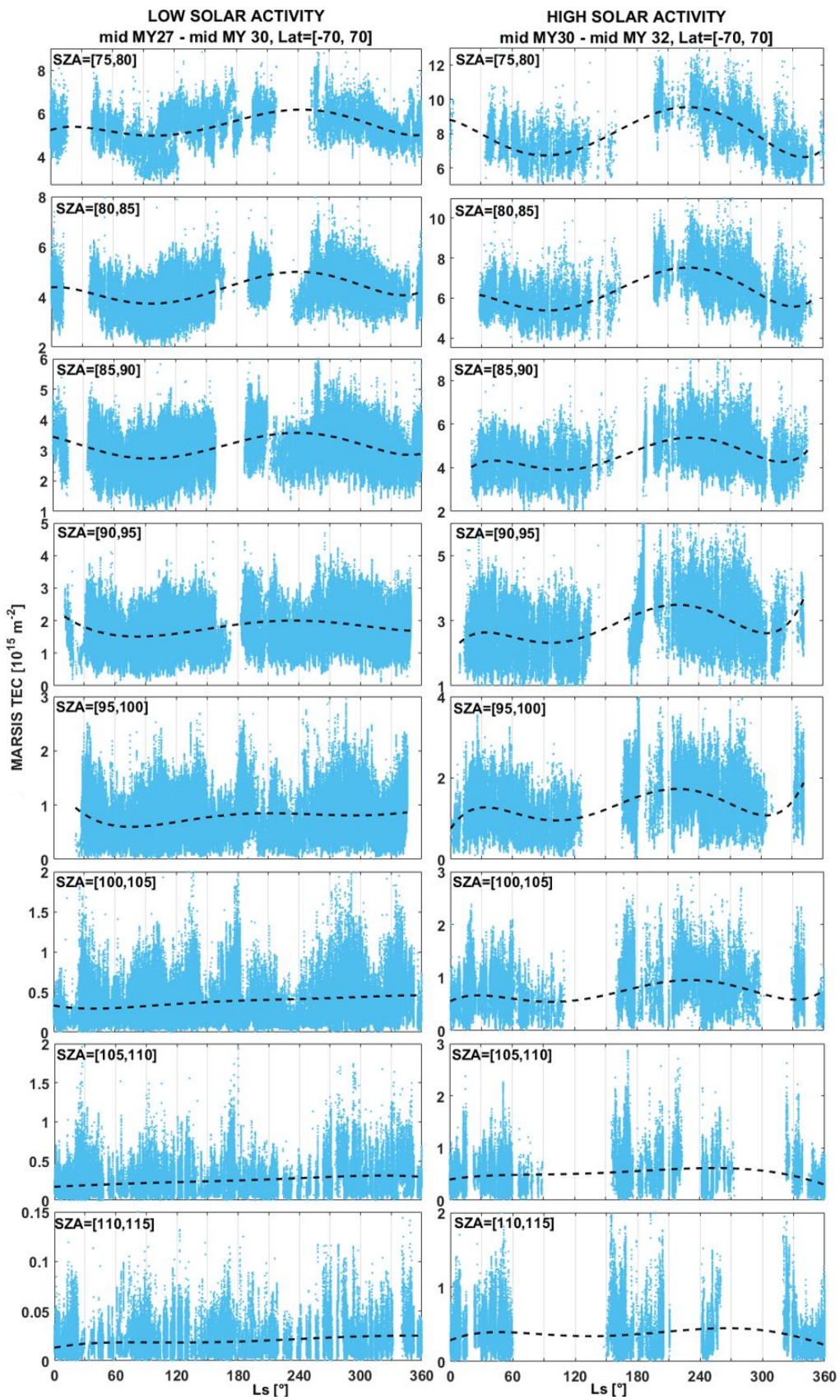
736

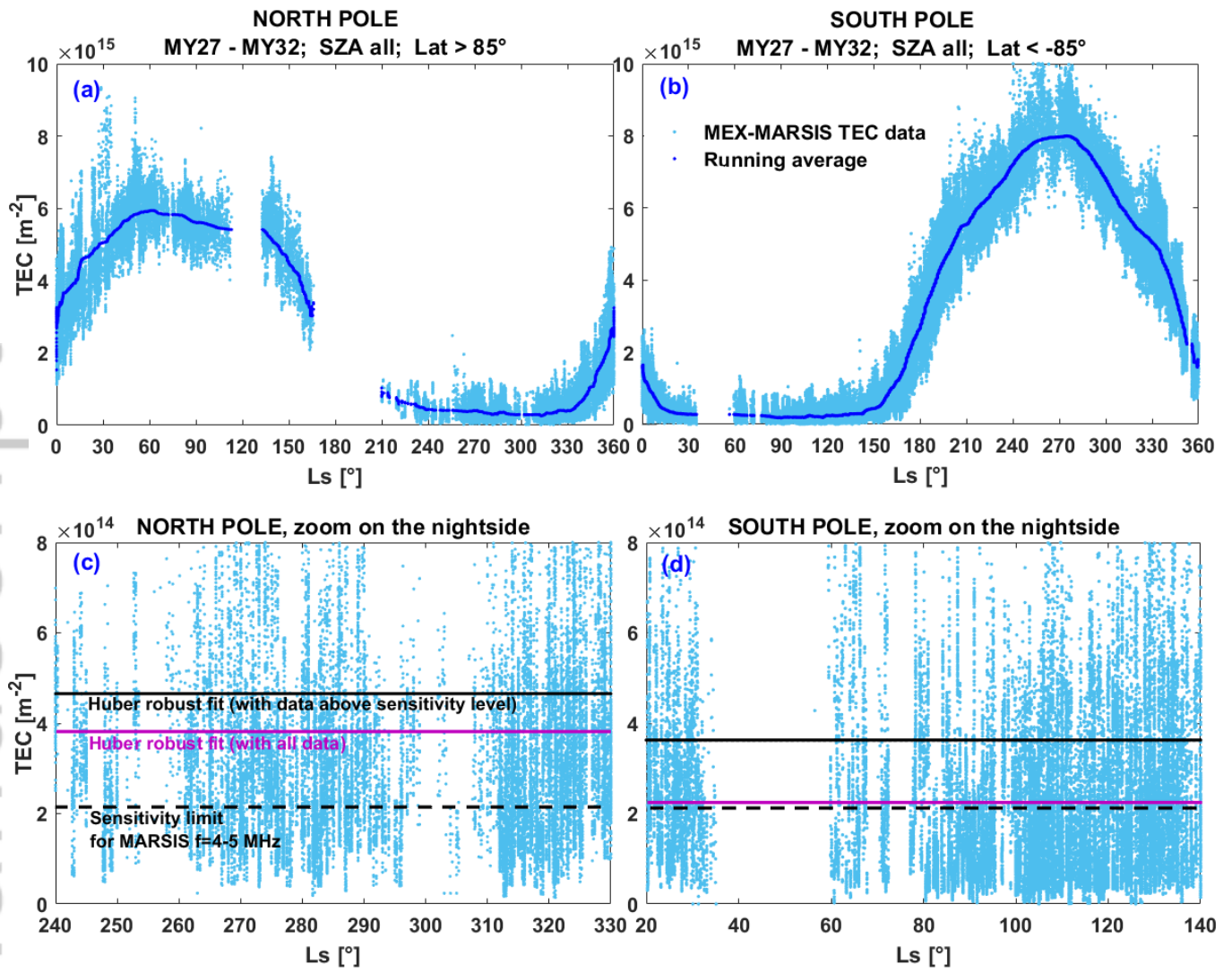
737

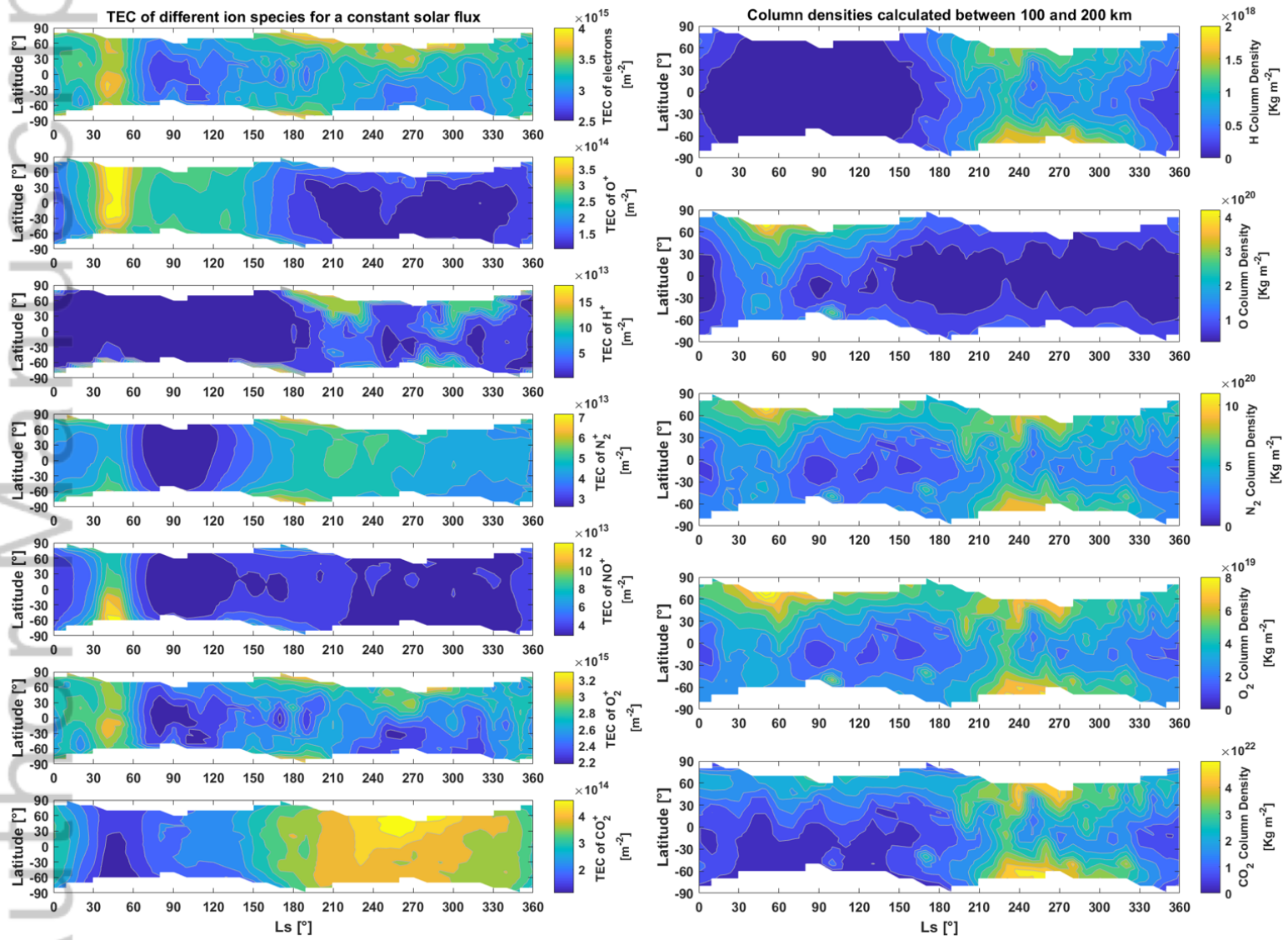
738

Figure 5: TEC contribution of each species for three different latitude bands, from the simulation of Figure 4. Each profile has been normalized by the corresponding TEC at each Ls.









2018JE005626-f04-z-.tif

